

Peritumoral Microgel Reservoir for Long-Term Light-Controlled Triple-Synergistic Treatment of Osteosarcoma with Single Ultra-Low Dose

Jiaqi Yan, Yichuan Wang, Meixin Ran, Rawand A. Mustafa, Huanhuan Luo, Jixiang Wang, Jan-Henrik Smått, Jessica M. Rosenholm, Wenguo Cui, Yong Lu,* Zhenpeng Guan,* and Hongbo Zhang*


Local minimally invasive injection of anticancer therapies is a compelling approach to maximize the utilization of drugs and reduce the systemic adverse drug effects. However, the clinical translation is still hampered by many challenges such as short residence time of therapeutic agents and the difficulty in achieving multi-modulation combination therapy. Herein, mesoporous silica-coated gold nanorods (AuNR@SiO₂) core-shell nanoparticles are fabricated to facilitate drug loading while rendering them photothermally responsive. Subsequently, AuNR@SiO₂ is anchored into a monodisperse photocrosslinkable gelatin (GelMA) microgel through one-step microfluidic technology. Chemotherapeutic drug doxorubicin (DOX) is loaded into AuNR@SiO₂ and 5,6-dimethylxanthenone-4-acetic acid (DMXAA) is loaded in the microgel layer. The osteosarcoma targeting ligand alendronate is conjugated to AuNR@SiO₂ to improve the tumor targeting. The microgel greatly improves the injectability since they can be dispersed in buffer and the injectability and degradability are adjustable by microfluidics during the fabrication. The drug release can, in turn, be modulated by multi-round light-trigger. Importantly, a single super low drug dose (1 mg kg⁻¹ DOX with 5 mg kg⁻¹ DMXAA) with peritumoral injection generates long-term therapeutic effect and significantly inhibited tumor growth in osteosarcoma bearing mice. Therefore, this nanocomposite@microgel system can act as a peritumoral reservoir for long-term effective osteosarcoma treatment.

1. Introduction

Chemotherapy is widely used in cancer treatment and the conventional anti-cancer drug administration is mostly achieved by oral administration and intravenous injection, which will cause the drug to be undistinctly distributed throughout the body, resulting in ineffective treatment and systemic toxicity.^[1] To achieve enhanced specific drug uptake in the tumor lesions, nanocarriers have been widely studied to achieve various sophisticated effects, including photothermal therapy,^[2] receptor-mediated targeting,^[3] multi-drug chemotherapy,^[4-6] and so forth. Dependent on the enhanced permeation and retention (EPR) effect, the tumor enrichment of anticancer therapies is indeed improved by nanocarriers after intravenous (IV) administration;^[7,8] however, the improvement is not significant, since the majority of the nanoparticles are still taken up by the liver and kidney.^[9-11] Hence, large doses and repeated administrations are still necessary to achieve long-term therapeutical effects.

J. Yan, M. Ran, Prof. W. Cui, Prof. Y. Lu, Prof. H. Zhang
Department of Radiology
Shanghai Institute of Traumatology and Orthopaedics
Ruijin Hospital LuWan Branch
Shanghai Jiao Tong University School of Medicine
149 ChongqingNan Road, Shanghai 200020, P. R. China
E-mail: 18917762053@163.com; hongbo.zhang@abo.fi

J. Yan, M. Ran, R. A. Mustafa, Dr. J. Wang, Prof. J. M. Rosenholm, Prof. H. Zhang
Pharmaceutical Sciences Laboratory
Faculty of Science and Engineering
Åbo Akademi University
Turku 20520, Finland

 The ORCID identification number(s) for the author(s) of this article can be found under <https://doi.org/10.1002/smll.202100479>.

© 2021 The Authors. Small published by Wiley-VCH GmbH. This is an open access article under the terms of the Creative Commons Attribution License, which permits use, distribution and reproduction in any medium, provided the original work is properly cited.

DOI: 10.1002/smll.202100479

J. Yan, M. Ran, Dr. J. Wang, Prof. H. Zhang
Turku Bioscience Centre
University of Turku and Åbo Akademi University
Turku 20520, Finland

Y. Wang, Prof. Z. Guan
Department of Orthopedics
Peking University Shougang Hospital
No.9 Jinyuanzhuang Rd, Shijingshan District, Beijing 100144, P. R. China
E-mail: guanzenpeng@qq.com

H. Luo
Jiaxing Key Laboratory of Basic Research and Clinical Translation on Orthopedic Biomaterials
Department of Orthopaedics
The Second Affiliated Hospital of Jiaxing University
Jiaxing 314000, P. R. China

Dr. J. H. Smått
Laboratory of Molecular Science and Engineering
Faculty of Science and Engineering
Åbo Akademi University
Turku 20520, Finland

In recent years, in order to maximize the efficiency of drug delivery, local therapy has received widespread attention.^[12–14] Compared with oral administration and intravenous injection, local minimally invasive administration can directly deliver agents into the tumor site through a controlled manner, which can greatly reduce the drug dose, thus sparing the off-target toxicity.^[14] However, the clinical translation of local therapy is still impeded by many well-known challenges: i) short retention time of therapeutic agents,^[7] ii) poor uptake of anticancer therapies by drug-resistant tumor cells, and iii) difficulty in realizing responsive multi-modal therapy. Therefore, to prepare a tumor receptor targetable formulation with adjustable in situ biodegradability and multi-modal combination treatment capabilities, through minimally invasive injection, is of great significance.

Gold nanorods (AuNRs) with tunable localized surface plasmon resonance (SPR) is widely used in the development of near infrared (NIR) responsive cell imaging and therapeutic platforms.^[15,16] The locally generated heat by NIR laser irradiation can not only achieve hyperthermia treatment, but also promote drug release and chemotherapy sensitization.^[17] Moreover, AuNRs can also achieve anti-tumor angiogenesis effect by targeting endothelial cell division process and disrupt cytokinesis through disturbing actin monomers assembly.^[18,19] However, bare AuNRs have several limitations in drug delivery, including 1) low drug loading capacity due to low surface area; 2) ease of aggregation and loss of deep-tissue response, since the NIR response window is very sensitive on the AuNRs size, and the growth in size will shift the NIR response window to the visible spectral region; 3) poor targeting and permeability due to limited possibilities to introduce targeting ligands on the surface. In order to overcome these defects, mesoporous silica with large surface area and flexibility in surface modification, is introduced to coat the AuNRs, to guarantee high drug loading capacity, protection of the AuNRs from aggregation, and enabling of ample surface functionalization possibilities with tumor targeting ligands.^[20,21] In this study, alendronate (ALN) is chosen for osteosarcoma targeting, introduced to the surface of AuRN@SiO₂ through EDC/sulfo-NHS coupling reaction (Scheme 1A). Therefore, the AuRN@SiO₂ core-shell nanosystem can realize effective anti-cancer drug loading, stable photothermal response, as well as enable the receptor-mediated endocytosis of cancer cells. Nevertheless, due to the small size, the AuRN@SiO₂ nanosystem does not have long-term retaining capability in tumor after local injection.

Hydrogels, on the other hand, with great in situ retention ability have been extensively studied as a non-toxic, non-immunogenic platform for tissue engineering and had been widely used for local therapy.^[22–24] GelMA hydrogel scaffold, fabricated by UV irradiating photo-initiator contained methacrylic anhydride (MA) conjugated gelatin, shows excellent biomechanical properties for extracellular matrix mimicking and high payload of hydrophilic therapeutic agents.

However, since GelMA based scaffolds are often used for cell-laden tissue engineering in bulk conditions,^[25,26] their injectability and degradation capabilities for local injection need to be further optimized.^[27,28] For example, to tightly host the drugs, the GelMA hydrogel must be dense, but if it is too dense, it is very difficult to inject. Furthermore, through traditional shearing, the injectability of GelMA can be improved,

but the therapeutic agents loaded inside will also suffer huge leaking. In light of this, AuRN@SiO₂-ALN NPs are sealed into monodisperse photocrosslinkable GelMA microgel by using a high-resolution controllable microfluidics technology. Through microfluidic technology, monodisperse microgels (abbreviated as NPs@GelMA) with different volumes and different degradation rates can be fabricated. The injectability can be greatly improved since the denser microgels can be dispersed in injection buffer for peritumoral injection (peritumoral injection). Moreover, coupled with the photothermal response and receptor-mediated targeting ability of the nanoparticles, the drug release and enhanced tumor cell uptake can be precisely controlled by the NPs@GelMA system.

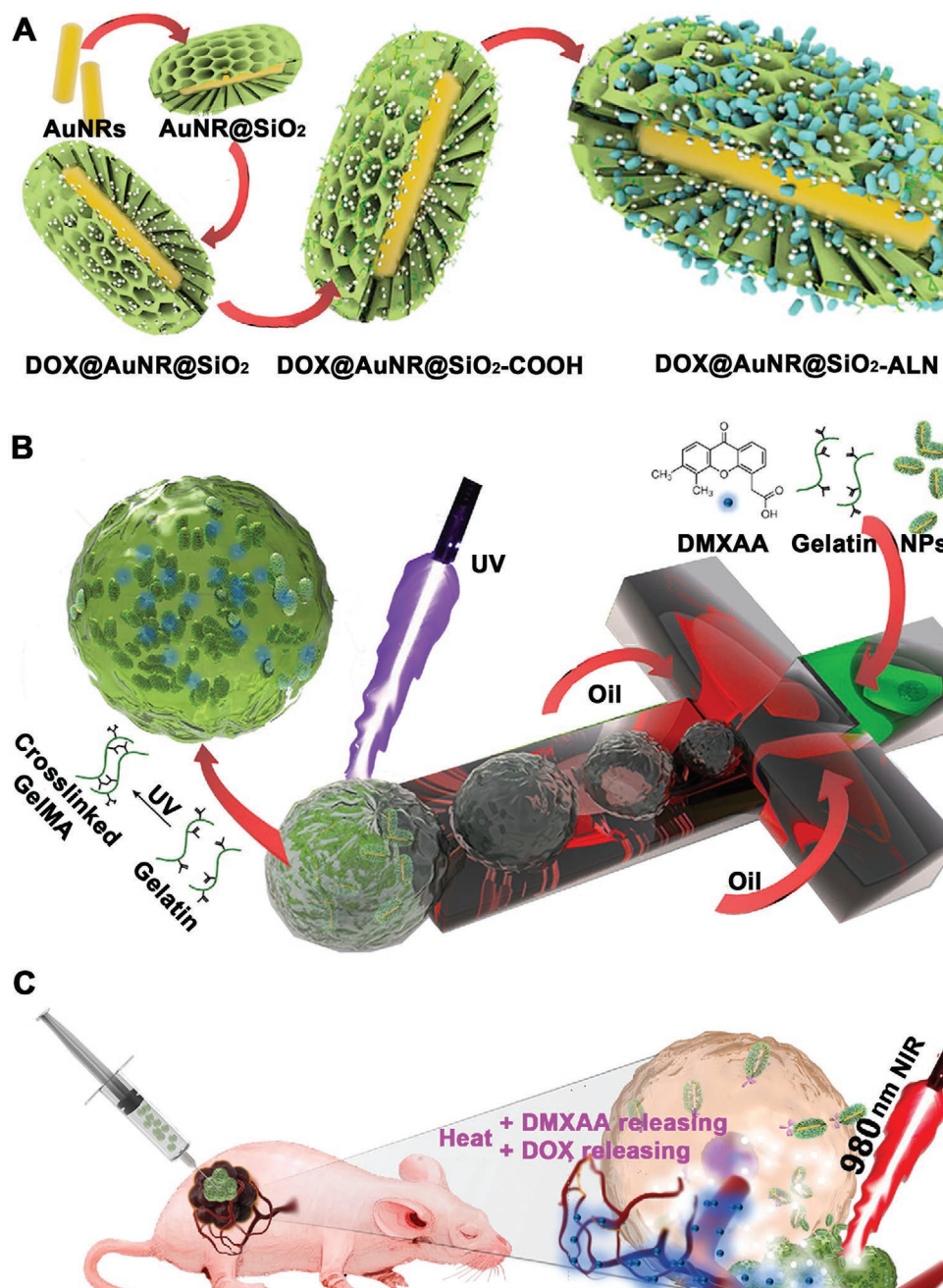
In this work, doxorubicin (DOX) and 5,6-dimethylxanthenone-4-acetic acid (DMXAA) were selected as model drugs to be loaded into AuRN@SiO₂-ALN NPs (NPs/DOX) and GelMA (GelMA/DMXAA) microgels, respectively. As an anthracycline anticancer drug, DOX is widely used because of its autofluorescence, which facilitates the detection of its in vitro and in vivo distribution.^[9] DMXAA, as a new type of small molecule vascular inhibitor in current clinical trials, can destroy the tumor vascular endothelial cells, cut off the tumor's oxygen and nutrient supply and prevent tumor metastasis.^[29] Combining these two different mechanisms, and the photothermal responsiveness of AuNRs, we anticipated to achieve chemo-antiangiogenesis-photothermal synergistic therapy for osteosarcoma treatment (Scheme 1B,C).

Consequently, the morphology, thermal conversion ability, and cell targeting ability of the nanoparticles were thoroughly studied in detail. The degradability of NPs/DOX@GelMA/DMXAA hydrogel with different volumes under 980 nm NIR laser irradiation was also investigated. The chemo-antiangiogenesis-photothermal combination therapeutic effect of this nanocomposite microgel, as well as biosafety of the NPs/DOX@GelMA/DMXAA system, are explored with osteosarcoma cells in vitro and osteosarcoma bearing mice in vivo through IV or peritumoral (PT) administration.

2. Results and Discussion

2.1. Synthesis and Characterization of Nanoparticles DOX@AuNR@SiO₂-ALN

Au nanorods with aspect ratio of ≈ 5 and average dimensions around 61 nm \times 12 nm were first synthesized according to a published procedure^[30] and then SiO₂ with a homogenous thickness of ≈ 11 nm was wrapped around the surface for DOX loading and ALN surface modification, as determined by transmission electron microscopy (TEM) (Scheme 1A; Figure S1, Supporting Information). The UV-vis absorption spectra showed that AuNRs had a longitudinal SPR peak at 849 nm and exhibited a red-shift to 889 after SiO₂ coating. A further red-shift to 917 was observed when DOX was loaded into the pores of SiO₂. (Figure S2A, Supporting Information) The TEM imaging and elemental mapping together showed that after SiO₂ coating, a mesoporous layer was formed on the surface of the AuNRs (Figure 1a–f). Subsequently, after drug loading and ALN surface decoration, the surface pores turned blurry (Figure 1c). In



Scheme 1. A) Fabrication of DOX@AuNR@SiO₂-ALN NPs. B) Fabrication of NPs /DOX@GelMA/DMXAA microgel. C) Nano-composite micro-gel with long-term therapeutic property controlled by repeatedly near-infrared-triggered release and combined with chemo-photothermal synergistic therapy.

addition, Fourier transform IR was implemented to verify the binding ability between ALN and NPs. After surface modification, we found that there is a new peak formed at 1633 cm⁻¹, which attribute to the C=O stretching of the new amide bond (Figure S3, Supporting Information). This result proved the effective combination of ALN with AuNR@SiO₂.

To investigate the photothermal effect of the NPs/DOX, different concentrations of NPs/DOX (0.25, 0.5, and 1 mg mL⁻¹) were irradiated with constant 980 nm laser (1 W cm⁻²) for 0–300 s (Figure 1g,h) and 0.5 mg mL⁻¹ NPs/DOX were irradiated under different laser powers (0.5, 1, and 1.5 W cm⁻²) for

0–300 s (Figure S4, Supporting Information). The photothermal response of the NPs/DOX exhibited positive correlation to concentration and laser intensity (Figure 1g,h; Figure S4, Supporting Information). With increased concentration of NPs/DOX and laser power intensity, the solution temperature rose rapidly. The temperature increased by 60 °C when 1 mg mL⁻¹ of NPs/DOX was irradiated for 300 s with 1 W cm⁻² laser intensity (Figure 1g,h), while pure water exhibited almost no temperature change under laser irradiation with the same intensity.

Moreover, the photostability and photothermal conversion efficiency (η) of NPs/DOX was also studied by conducting three

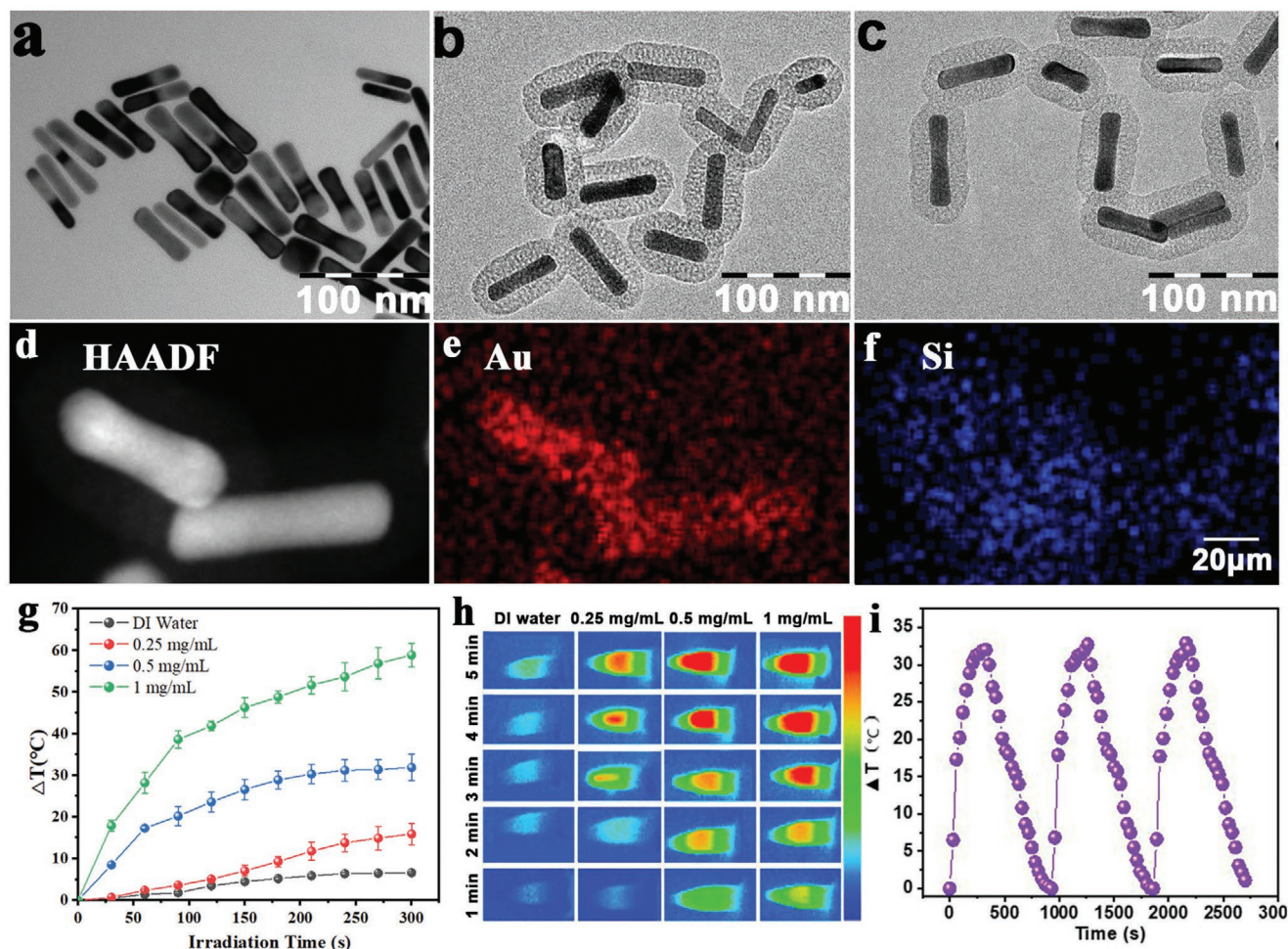


Figure 1. Characterization of nanoparticle morphology and photothermal effect. a–c) TEM of AuNRs, AuNR@SiO₂ NPs, and DOX@AuNR@SiO₂-ALN NPs. d–f) The high-angle annular dark-field imaging and elemental mapping of AuNR@SiO₂ NPs. g) Photothermal heating curves of DI water and AuNR@SiO₂ NPs with different nanoparticle concentrations (0.25, 0.5, and 1 mg mL⁻¹) under 1.0 W cm⁻², 980 nm laser irradiation. h) The infrared thermal images of DI water and AuNR@SiO₂ NPs with different nanoparticle concentrations under 1.0 W cm⁻², 980 nm laser irradiation. i) Temperature elevation of AuNR@SiO₂ NPs (0.5 mg mL⁻¹) over three times of NIR on–off irradiated cycles (1.0 W cm⁻², 980 nm).

heating–cooling cycles (Figure 1i) whereby the photothermal conversion efficiency of NPs/DOX was calculated as 27% from the heating–cooling curves. (Figure 1i; Figure S5, Supporting Information) The (η) was calculated based on Equations (1) and (2):^[31]

$$\eta = \frac{hs\Delta T_{\max} - Q}{I(1 - 10^{-A^{980}})} \quad (1)$$

Here, ΔT_{\max} is the maximum value of temperature change, Q is the heat increase of the solvent, and I is the power of the laser. A^{980} is the absorbance of the NPs/DOX at the wavelength of 980 nm, while hs can be calculated by another formula:

$$hs = \frac{mc}{\tau} \quad (2)$$

Here, c and m are the specific heat capacity and mass of the solution, respectively. τ is the slope of the fitted line of t to $-\ln \frac{\Delta T}{\Delta T_{\max}}$.

Subsequently, Brunauer–Emmett–Teller analysis gave the nitrogen adsorption–desorption isotherms and pore size distribution curves of AuNRs@SiO₂. The pore size was mainly distributed in 2.3 nm, and the specific surface area was as high as 308 m² g⁻¹ (Figure S6, Supporting Information). These results indicated that the nanoparticles possessed sufficient size and space for drug loading. The loading content (LC) of DOX in AuNRs@SiO₂ was 30.0 ± 6.7%, as quantified by UV–vis absorption at 490 nm (Table S1, Figure S2B, Supporting Information). For studying the drug release, the light-controlled drug release effect of NPs/DOX was confirmed by three times of NIR on–off irradiated cycles (Figure S7, Supporting Information), since the generated heat by PTT will weaken the interaction between DOX and silica. The releasing profiles showed that when laser was applied, a burst release (29.8%) at first 5 min irradiation was observed, then 20.8% and 21.1% DOX releasing was founded at second and third round of irradiation. While, without laser irradiation, only 10% of DOX released from the AuNRs@SiO₂ after 6 h. These results proved that DOX@AuNR@SiO₂-ALN NPs possessed great PTT effect and had NIR triggered drug releasing ability.

Finally, we investigated the size distribution of AuNR@SiO₂, DOX@AuNR@SiO₂, and DOX@AuNR@SiO₂-ALN NPs, as well as the dispersibility and stability of AuNR@SiO₂ NPs in the PBS buffer and Milli-Q water. The results shown that the NPs exhibited very good dispersibility in Milli-Q water, with size of 120.2 ± 17.5, 122.3 ± 10.9, and 130.7 ± 18.5 nm for AuNR@SiO₂, DOX@AuNR@SiO₂, and DOX@AuNR@SiO₂-ALN, respectively; however, the size increased to 354.5 ± 76.5, 357.5 ± 68.5, and 374.3 ± 52.4 nm in PBS, as shown in Figure S8, Supporting Information. In addition, long-term stability studies have shown that Au@MSN nanoparticles gradually aggregated in PBS buffer. After 7 days of incubation, the TEM results proved the degradability of the NPs under PBS buffer, while the NPs removed unchanged in Milli-Q water (Figure S9A,B, Supporting Information). In our designed microgel reservoir system, the NPs were loaded into the microgel in Milli-Q water, therefore this can protect the NPs from aggregation and significantly improve the NPs' bioavailability.

2.2. Synthesis and Characterization of NPs/DOX@GelMA/DMXAA Microgel

Gelatin methacrylate, as a photocrosslinkable hydrogel has been widely studied as cell scaffolds and wearable devices due to its excellent biocompatibility.^[32,33] Cells and drugs can be loaded into the GelMA solution before UV curing, or absorbed by the surface (microscale) and internal (nanoscale) pores of crosslinked GelMA hydrogel. However, for bulk GelMA hydrogel it has been challenging to achieve adjustable in situ degradability and shown to be difficult to be applied in minimally invasive applications. Therefore, herein we utilized microfluidic technology to prepare different sizes of injectable GelMA microgels that can not only achieve different degradability profiles, but also retain bulk gel properties. First, by controlling the flow rate of the internal phase (GelMA, photo-initiator) and external phase (mineral oil, Span 80) in microfluidics, we can easily fabricate monodisperse microspheres with particle size of 265 ± 20, 160 ± 24, and 50 ± 15 μm (aqueous:oil = 1:1, 1:2, and 1:3, respectively) (Figure 2a). Then, the nanohybrid microspheres were collected and crosslinked by UV (20 mW cm⁻²d⁻¹, 480 nm) for 20 s.

Subsequently, the degradation rate of nano-hybrid microgels was investigated from three aspects, including the size of the microgel, the LC of NPs/DOX and DMXAA, as well as the laser induced light-triggered degradation. It has been reported that the mechanical strength of GelMA hydrogel increases with mesoporous silica or gold nanorod incorporation since the internal porosity will decrease, thereby prolonging its degradation and drug release time.^[34] Moreover, since the microgels still retained bulk gel properties and the crosslinking ability of GelMA solution will not change due to the different crosslinking shape and size, the bulk hydrogel was used to simulate the microgel and investigate the best LC of NPs/DOX and DMXAA.

In this work, we can easily prepare GelMA hydrogels with different concentrations of NPs/DOX and DMXAA (Figure 2b). The NPs contained 30% of DOX, and we fixed DOX to DMXAA ratio to 1:3 to maximize the synergistic effect, according to the

previous article.^[9,29] We found that the GelMA hydrogel could resist increased crushing force by loading 5 mg mL⁻¹ NPs/DOX and 4.5 mg mL⁻¹ of DMXAA, and the resistance further increased to 125 ± 11 g crushing force by loading 10 mg mL⁻¹ of NPs/DOX and 9 mg mL⁻¹ DMXAA. However, the GelMA hydrogel completely lost the resistance of crushing force when 15 mg mL⁻¹ of NPs/DOX and 13.5 mg mL⁻¹ DMXAA were loaded, since large amount of NPs/DOX and DMXAA destroyed the basic skeleton of GelMA hydrogel and the GelMA could not crosslink to a stable structure (Figure 2b). Based on these results, 10 mg mL⁻¹ NPs/DOX (3 mg mL⁻¹ DOX) together with 9 mg mL⁻¹ DMXAA were chosen and loaded into GelMA to fabricate the NPs/DOX@GelMA/DMXAA microgel with different sizes through microfluidics (Figure 2c).

We then used confocal to evaluate the NPs' distribution in the microgel. First we chemically conjugated Cy5.5-NHS to the surface of the AuNR@MSN-NH₂ NPs to prevent the dye releasing. By ultrasonic cleaning, we cleaned the free dye which adsorbed inside the nanoparticle pores. Then we added small amount of FITC inside the gel-NPs solution as the internal phase for the microfluidics. When preparing microgel spheres by microfluidic technology, in order to prevent the fusion of droplets, span 80 was added as a surfactant, which extracted FITC to the outer layer of the microgel. By merging the two types of fluorescence together, we could visually see the distribution of fluorescent nanoparticles inside the microgel. The FITC formed a green halo to exhibit the microgel. The Cy5.5 conjugated NPs distributed evenly inside the microgel (Figure 2d).

Subsequently, the degradation curves of different sizes of NPs/DOX@GelMA/DMXAA microgels prepared under different aqueous:oil flow rates (1:1, 1:2, and 1:3) were monitored (Figure 2e). We found that during the initial 6 days of laser-free incubation, the hydrogel showed 7 ± 2.4% degradation for the 1:1 group. However, for 1:2 and 1:3 groups, there were 13 ± 1.8% and 37 ± 3% of the mass lost within 6 days, respectively, which suggested that the degradation rate of the microgel will gradually extend as the microgel size increased and the surface area decreased. Moreover, after irradiated by 980 nm laser (1 W cm⁻²) for 10 min on the 6th and 12th day, the results showed that the three groups all exhibited multiple rounds of light-induced accelerated degradation, while the degradation time of the 1:1 group was longer than the other groups and up to 24 days, which may satisfy the long-term treatment purpose. Therefore, we chose 1:1 as the optimal flow rate to prepare a microgel with a particle size of around 265 μm.

Later, the NPs/DOX@GelMA/DMXAA microgel was freeze dried and observed under a fluorescent confocal microscope. The results showed that the microgel exhibited a uniform size, and there were abundant pores on the surface, which facilitated the media exchange between microgels and tumor microenvironment in vivo (Figure 2f,g). Furthermore, DOX and DMXAA release profiles were also calculated by UV absorbance at 490 and 350 nm (Figure 2h; Figure S2B, Supporting Information). After irradiation by 980 nm laser (1 W cm⁻²) for 10 min on the 6th and 12th day, accelerated release of DOX and DMXAA was found. Meanwhile, 90 ± 4% of DMXAA and 74 ± 5% of DOX were released during 24 days. These results proved that the NPs/DOX@GelMA/DMXAA microgel system possessed great

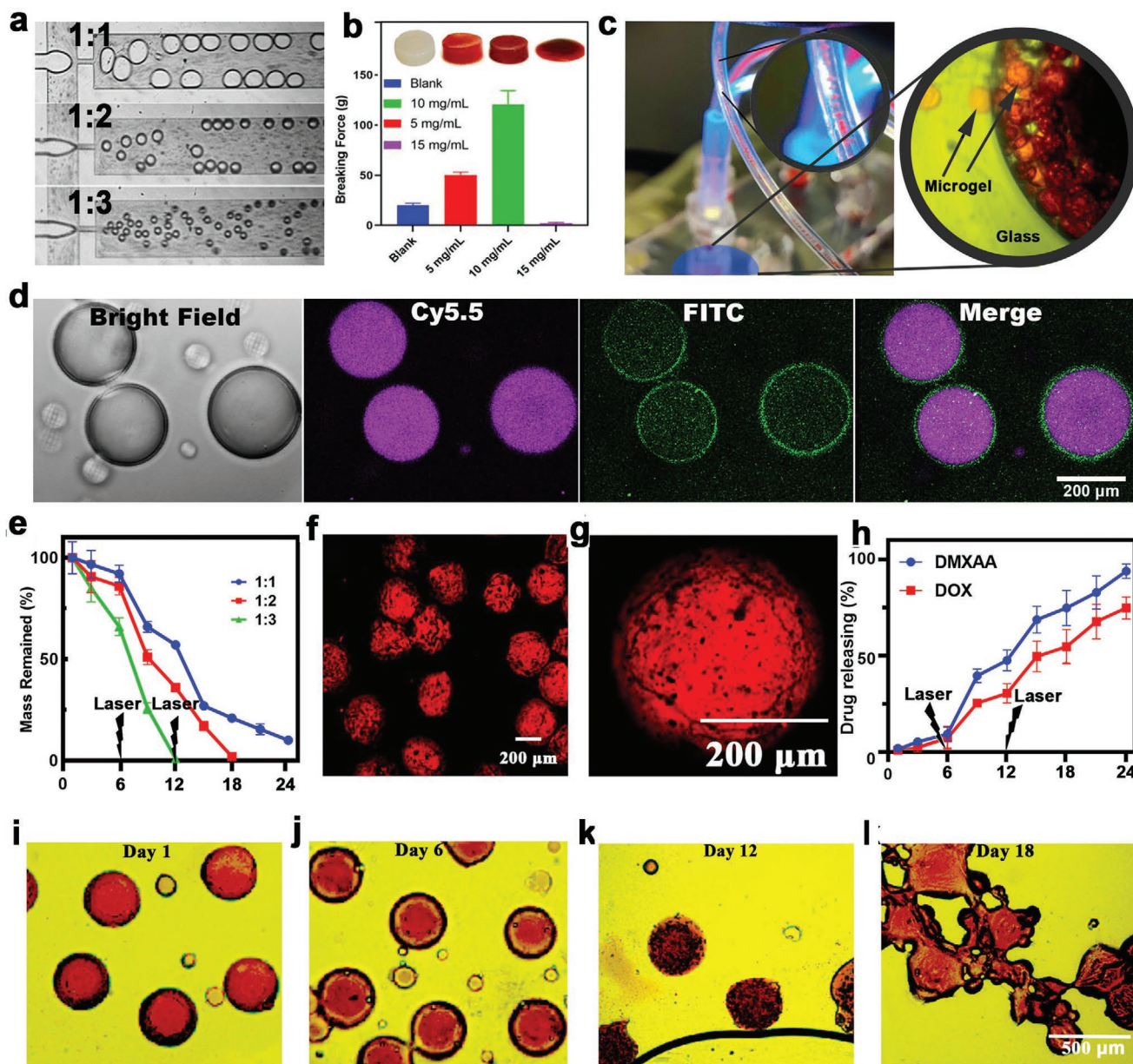


Figure 2. Characterization of microgel morphology. a) The microscope images of microgels within microfluidic chips under different aqueous:oil flow rates (1:1, 1:2, and 1:3). b) Photos and breaking forces of GelMA hydrogel which bearing different concentrations of NPs/DOX and DMXAA. c) NPs/DOX and DMXAA loaded microgels within microfluidic outlet tube and enriched in the reservoir. d) Co-localization test of nanoparticles and hydrogel. e) The degradation curve of NPs/DOX@GelMA/DMXAA microgel under different aqueous:oil flow rates (1:1, 1:2, and 1:3). f, g) Fluorescence microscope image of dispersed freeze-dried NPs/DOX and DMXAA loaded microgels and the mono-microgel. h) The accumulated drug releasing of DMXAA and DOX of microgel which fabricated under 1:1 aqueous:oil flow ratio. i–l) Fluorescence images of the NPs/DOX@GelMA/DMXAA over three weeks under different time-point NIR irradiation.

light-controlled drug release ability and long-term degradability. In addition, fluorescence microscopy was also used to observe the morphology of microgel on the 1st, 6th, 9th, and 18th day. As shown in Figure 2i–l, the shape of the red microgel hardly changed in the first 6 days, but after the laser irradiation on the 6th day, we observed significantly different phenomena on the 12th day. First, the drug was released in a burst fashion between the 6th and the 12th day (Figure S10A, Supporting Information). Second, the flattened surface of the microgel (Figure 2i;

Figure S10B, Supporting Information) became uneven on the 12th day, showing dense pores on the surface (Figure 2k; Figure S10C, Supporting Information). These pores may be induced by the heat-triggered GelMA degradation that was produced by nanoparticles inside the microgel. Therefore, these results once again confirmed this nano-hybrid microgel system possessed long-term controllability of precision photothermal therapy and accurate NIR-triggered drug release capability from the macroscopic morphology aspect.

2.3. Targeting and Cytotoxicity Evaluation of NPs/DOX and NPs/DOX@GelMA/DMXAA Microgel on Osteosarcoma Cells

In order to evaluate the therapeutic ability of the nanocomposite microgel in vitro, the targeting ability and tumor cell toxicity of the NPs/DOX, as well as the tumor cell suppression capacity of NPs/DOX@GelMA/DMXAA microgel were carried out through fluorescence microscopy imaging and CCK-8 experiments. First, the confocal laser scanning microscopy (CLSM) images showed that after the ALN modification, DOX@AuRN@SiO₂-ALN group exhibited much higher uptake efficiency compared with the undecorated DOX@AuRN@SiO₂ group, as shown in **Figure 3a**. Moreover, after laser irradiation, we found more drugs can penetrate into the nuclear space, while within the laser-absent group, the NPs/DOX can only accumulate surrounding the nucleus, which means a lesser degree of drug released, since the DOX will enter the nucleus to exert its effects (**Figure 3a**). These phenomena proved that the DOX@AuRN@SiO₂-ALN NPs not only had great uptake ability, but also held excellent NIR sensitivity.

Later, CCK-8 based cytotoxicity was conducted. From the results we can see that the laser induction group demonstrated stronger tumor killing ability when the DOX concentration exceeded 1 $\mu\text{g mL}^{-1}$ (**Figure 3b**). Then, with the DOX concentration of 10 $\mu\text{g mL}^{-1}$, more than 85% of the cells was inhibited in the DOX@AuRN@SiO₂-ALN +Laser group, which was more effective than the pure DOX and DOX@AuRN@SiO₂ +Laser groups. The results suggested that the ALN modified NPs/DOX system possessed the greatest tumor inhibiting ability, which was contributed to by the laser-triggered PTT effect and the ALN receptor mediated enhanced uptake.

Subsequently, through a live/dead cell staining experiment, we studied the cytotoxicity of NPs/DOX and DMXAA dual loaded microgel systems. From **Figure 3c** we can see that for control and NPs/DOX@GelMA/DMXAA –Laser group, there were negligible dead (red) cells exist after 24 h incubation, which showed less toxicity than pure DOX group. However, after these microgels were laser irradiated, almost all MNNG/HOS osteosarcoma cells died within 24 h. Also, from the local irradiation results, we can clearly see that cells can only be killed where the laser hit (**Figure S11**, Supporting Information). These results confirmed that this microgel system possessed great safety unless it had been triggered by NIR laser. Finally, flow cytometry was also used for the detection of the cell apoptosis of each group. The results showed that NPs/DOX@GelMA/DMXAA +Laser group exhibited the highest number of apoptotic cells (21.5% dead and 15.7% late-apoptotic cells) (**Figure 3d**), and showed the best therapeutic effect that corresponded with the dead/live experiment.

2.4. Tumor Vascular Disruption

Tumor angiogenesis is a hallmark feature of solid tumors. During tumor growth, a large number of new blood vessels can not only provide nutrients and remove waste from the tumor, but also provide a transport pathway for the distant metastasis of the tumor. Therefore, to complement the current chemotherapy, it is important to develop new methods to effectively

inhibit tumor angiogenesis. DMXAA, as one of the typical small molecule vascular disrupting agents can selectively target tumor vascular endothelium and destroy tumor blood vessels, and has been widely applied for clinic research.^[29] Moreover, nonlethal heat treatment of vascular endothelial cells can also inhibit the expression of adhesion molecules and may inhibit tumor growth by interfering with vascular supply.^[18] Consequently, in this experiment, while using the AuNRs to achieve PTT, DMXAA was also added to the microgel to achieve a dual effect of inhibiting blood vessels.

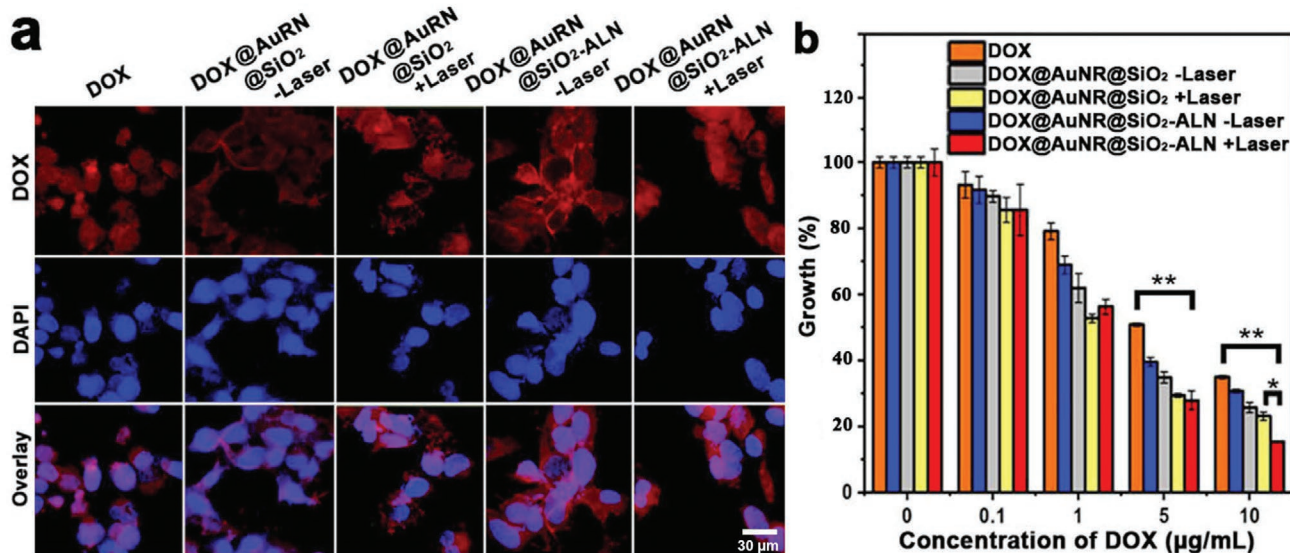
In the first step of studying the laser-induced inhibition of capillary formation, we used MNNG/HOS cell conditioned medium to stimulate the human umbilical vein endothelial cells (HUVEC), since the inflammatory factors in the tumor microenvironment can promote angiogenesis effect and affect the results of subsequent inhibition experiments.^[18] Then, different groups including: Control; NPs/DOX –Laser; NPs/DOX +Laser; NPs/DOX@GelMA/DMXAA –Laser; and NPs/DOX@GelMA/DMXAA +Laser group were tested for their antiangiogenic ability. The results showed that for each drug delivery system, the anti-capillary effect can be achieved only after laser was used (**Figure 4a**). Moreover, the NPs/DOX@GelMA/DMXAA +Laser group showed more inhibitability than pure NPs/DOX group which due to the synergistic therapy of both PTT and DMXAA vascular disturbing effect (**Figure 4a**). Furthermore, we also analyzed three major parameters through NIH ImageJ analysis:^[35] number of junctions (red spot), number of meshes (blue circle) and total length (yellow lines) of in vitro angiogenesis, as shown in **Figure 4b–d**. These three indicators can reflect the vigorous degree of angiogenesis. The more junctions and meshes and the longer the total length, the more vigorous blood vessels grow. Hence, from these results, we can see that for NPs/DOX@GelMA/DMXAA groups, the number of junctions decreased ten times after laser was used (**Figure 4b**), which confirmed near-infrared responsive vascular inhibition. Moreover, the number of meshes and total length results showed that NPs/DOX@GelMA/DMXAA +Laser group had less meshes (zero mesh) (**Figure 4c**) and 10% shorter length than NPs/DOX +Laser group (**Figure 4d**), which again proved the synergistic therapy of both PTT and DMXAA vascular disturbing effect.

2.5. Biodistribution of NPs/DOX and DOX Retention Ability In Vivo

Tumor-bearing mice were constructed by subcutaneous injection of MNNG/HOS cells for investigating the PTT effects of the formulation and drug distribution. It was found that after PT, the PTT effect of NPs/DOX@GelMA/DMXAA (PT) group was much higher than the PBS (PT) group and NPs/DOX (IV) group (**Figure 5a,b**; **Figure S12a,b**, Supporting Information). After 10 min irradiation of 980 nm laser (1 W cm⁻²), both of the NPs/DOX (IV) and NPs/DOX@GelMA/DMXAA (PT) group can be heated above 42 °C, where the cancer cells can be effectively killed.

Afterward, the fate of each formulation was examined through in vivo and in vitro fluorescence imaging experiments. Normally, the targeting efficiency of targeted formulations

Evaluation of the targeting ability and cytotoxicity of NPs on MNNG/HOS osteosarcoma cells



Cytotoxicity assess of NPs-hybridized microgel on MNNG/HOS osteosarcoma cells

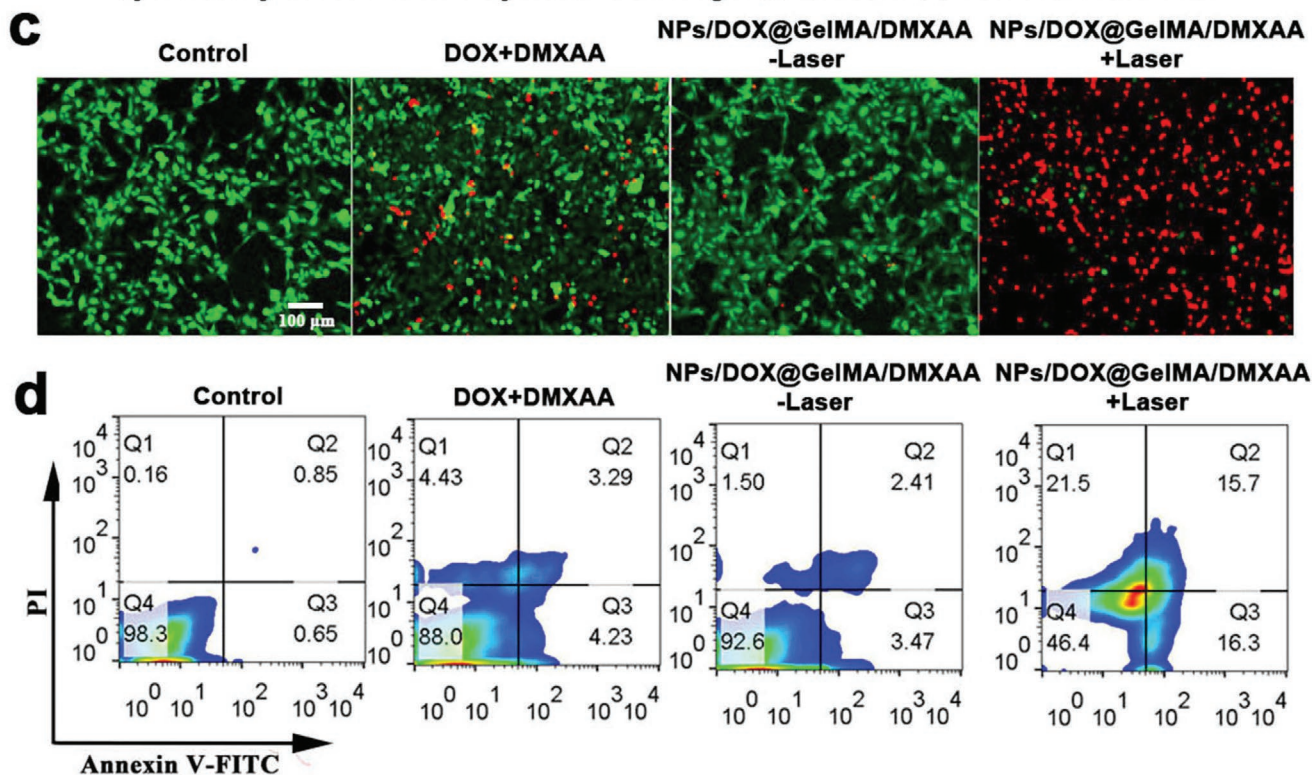


Figure 3. In vitro cell viability of osteosarcoma Silicatecells MNNG/HOS. a,b) The cell uptake experiments and CCK-8 cell toxicity assessment. c) Fluorescence microscope images of the live/dead cell staining assay of control, DOX+DMXAA, and NPs/DOX@GelMA/DMXAA (with or without laser) microgel groups. d) Flow cytometric apoptosis analysis of tumor cells under Annexin V-FITC/PI stained ($n = 3$, * $p < 0.05$ and ** $p < 0.01$).

designed through the EPR effect will not exceed 5%.^[36] Thus, in order to prove that the delivery efficiency of PT injection is much higher than that of IV administration, 1 mg kg⁻¹ DOX and 3 mg kg⁻¹ DMXAA were delivered, which only 20% of

the doses relative to IV administration.^[9,29] Obviously, after reducing the dosage, the NPs/DOX (IV) group showed only little fluorescences gathered around the tumor (Figure S12c, Supporting Information). Then for pure DOX (PT) group, DOX

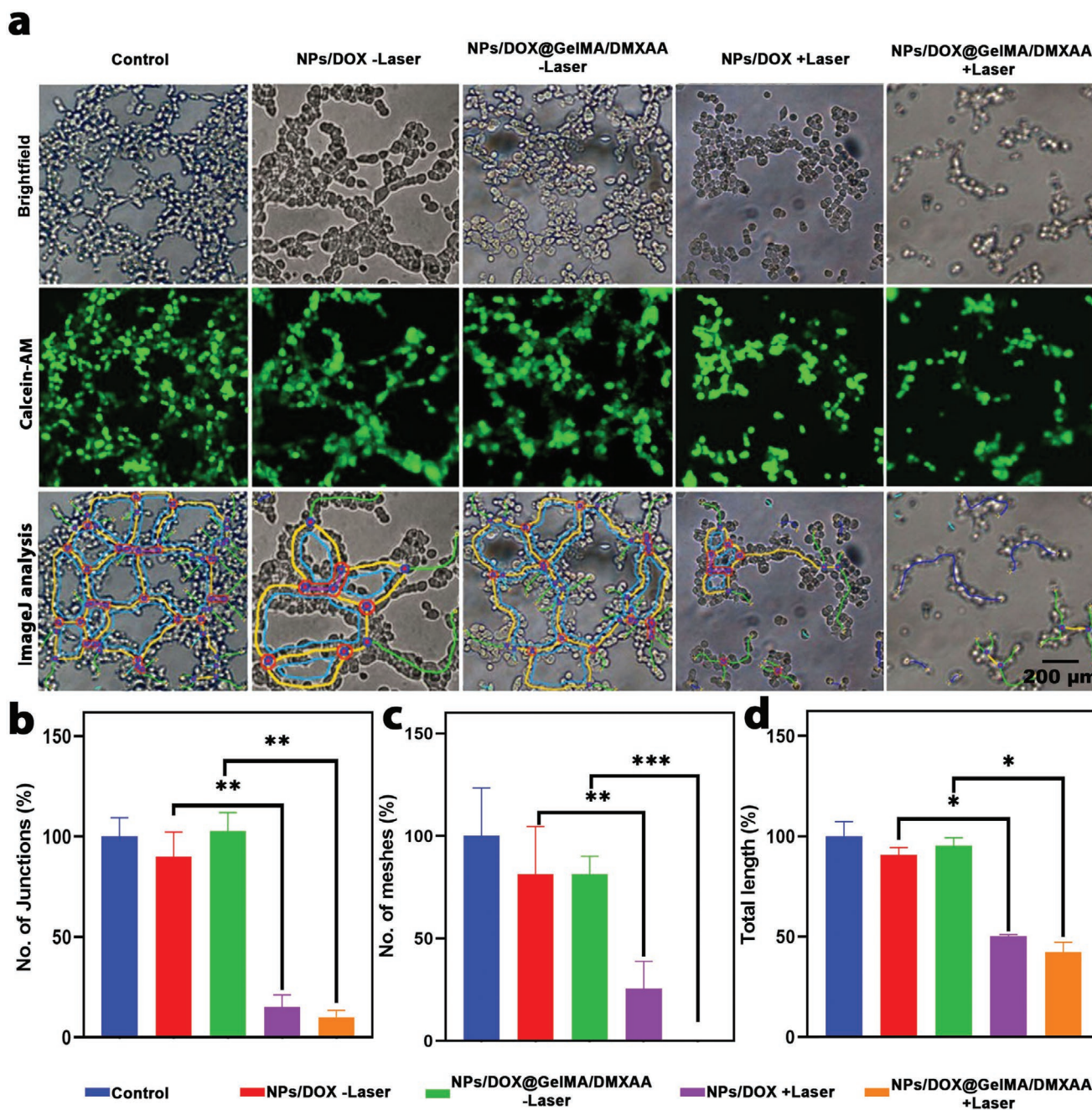


Figure 4. The inhibition experiments of angiogenesis. a) Tube formation effect of HUVEC and angiogenesis analyze results from ImageJ software for Control, NPs/DOX, NPs/DOX@GelMA/DMXAA, NPs/DOX +Laser, and NPs/DOX@GelMA/DMXAA +Laser groups, respectively (all scale bar equal to 200 μm). b–d) Comparison of number of junction, meshes, and total length between different groups by using ImageJ plugins Angiogenesis Analyze ($n = 3$, * $p < 0.05$, ** $p < 0.01$, and *** $p < 0.001$).

was more likely to spread to the surrounding tissues rather than inside the solid tumor (Figure 5c). Furthermore, the DOX within both NPs/DOX (IV) and DOX (PT) groups only stayed in the body for a short time and were basically eliminated by metabolism in 3 days. Therefore, in the cases of simple intratumoral injection of drugs or 1/5 dose of NPs/DOX tail vein injection, the drugs cannot effectively enter the tumor site.

By contrast, for NPs/DOX@GelMA/DMXAA group, we can see that without laser irradiation, the hydrogel was kept

at the tumor site and remained unchanged for half a month (Figure 5c). However, after 10 min of laser irradiation every three days, we found DOX had spread into the tumor. The fluorescence intensity of tumor in NPs/DOX@GelMA/DMXAA (PT) group was 5.8-folds higher than DOX (PT) group and DOX/NPs group (Figure 5d,e; Figure S12d,e, Supporting Information). These results proved the excellent drug delivery efficiency, sensitive near-infrared responsive drug release ability, and the tumor-enhancing phagocytosis of the nanoparticle-loaded microgels.

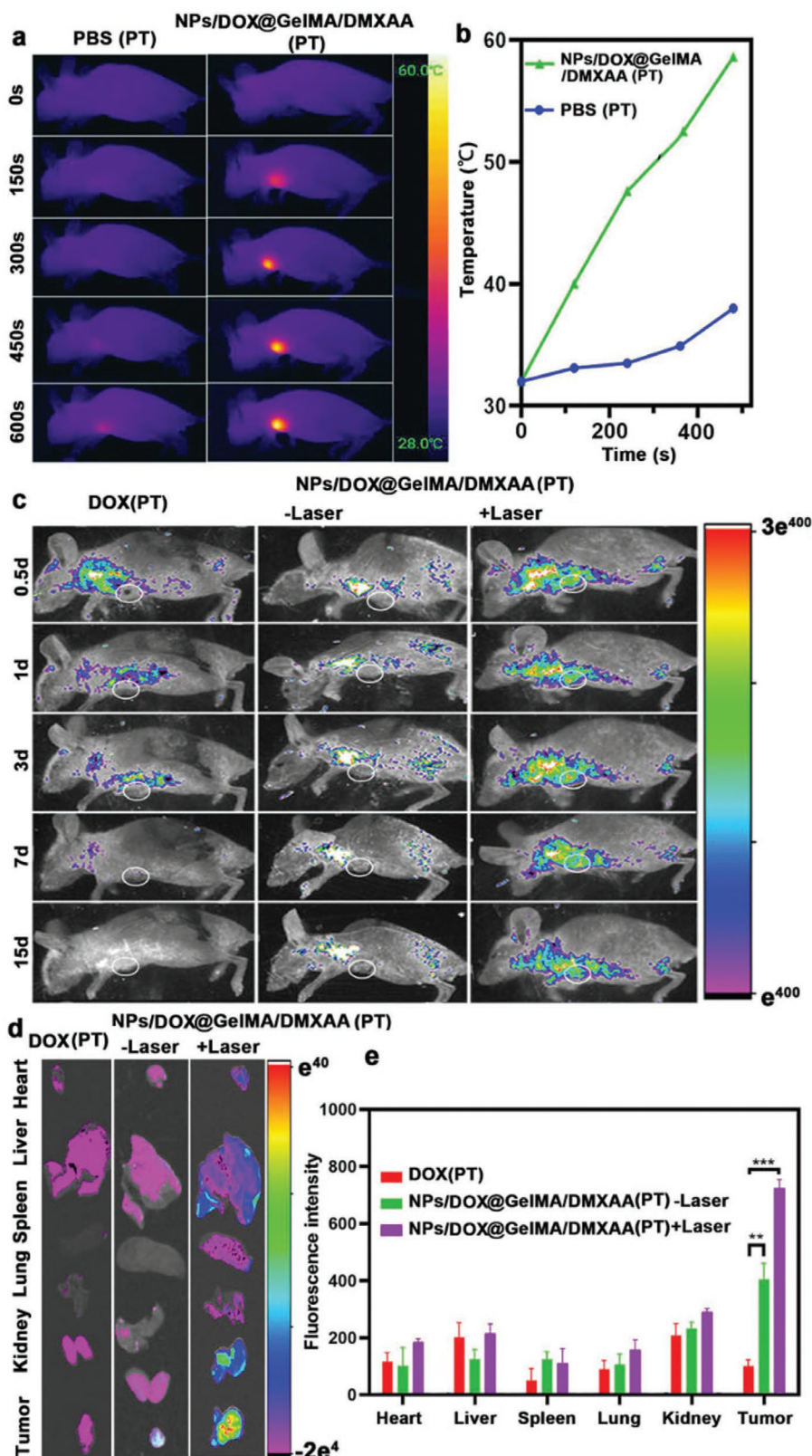


Figure 5. Thermal imaging photos of tumor bearing mice and the in vivo and in vitro doxorubicin biodistribution. a) Infrared thermal images of the tumor bearing mice at each time point while the tumor was continually irradiated by the 980 nm laser (1 W cm^{-2}) for 10 min. b) Time–temperature curve of the tumors from the mice after peritumoral (PBS, NPs/DOX@GelMA/DMXAA microgel) injection. c,d) In vivo and in vitro NIRF imaging of DOX fluorescence. e) Fluorescence intensity of DOX within different organs ($n = 3$, * $p < 0.05$ and *** $p < 0.001$).

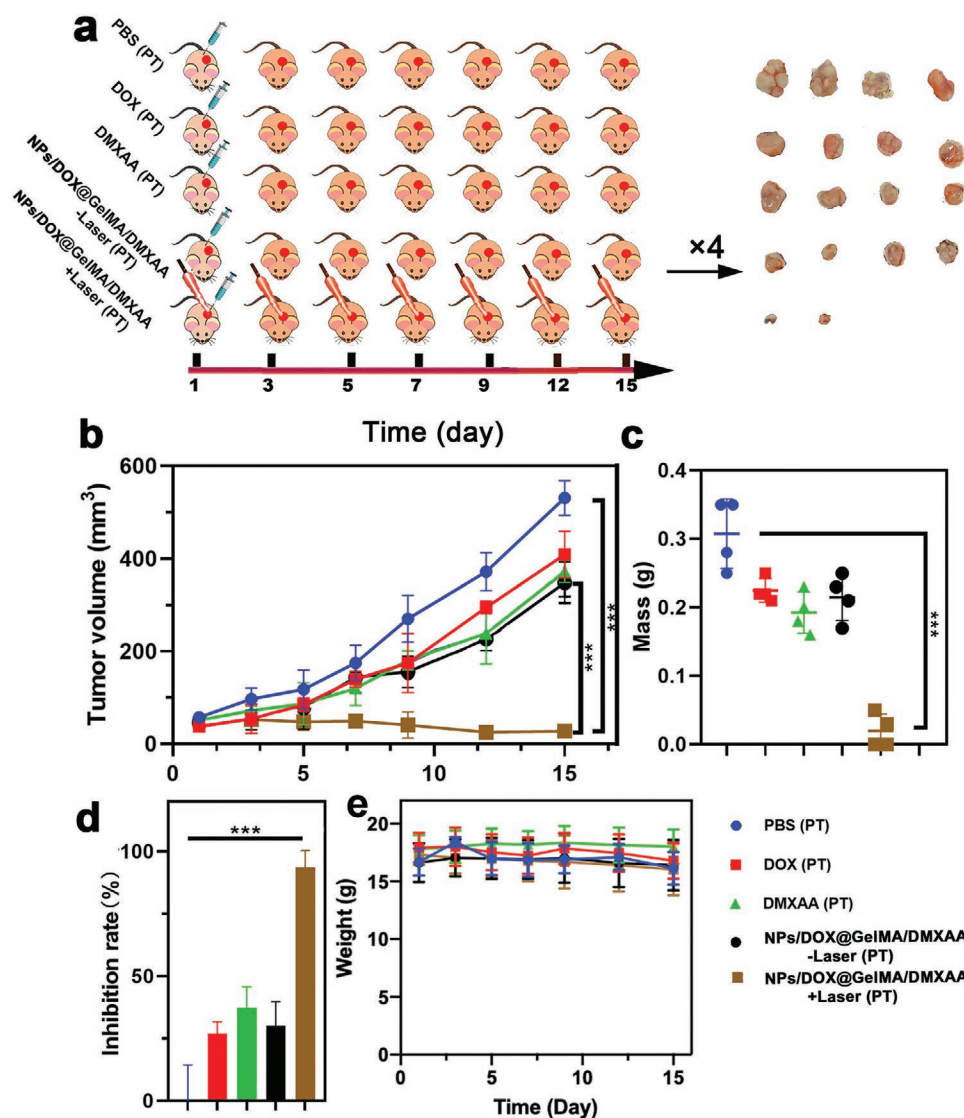


Figure 6. Treatments of tumors after peritumoral administration. a) Schematic diagram of the experimental design and the extracted tumor photos after the treatment. b) Tumor volume changes during the 15 days therapy. c) Mass of extracted tumors of different groups on 15th day. d) Tumor inhibition rates of different groups at 15th day. e) Body weight changes during 15 days therapy. ($n = 4$, $**p < 0.01$ and $***p < 0.001$).

2.6. In Vivo Tumor Inhibition Efficiency and Biosafety of Different Formulations

Encouraged by the gratifying tumor penetration ability of the nanocomposite microgel in vivo, we further verified the tumor inhibition capacity of different preparations, through seven groups of MNNG/HOS osteosarcoma xenograft tumor-bearing mice. For +Laser groups, the 980 nm laser (1 W cm^{-2}) was used for 10 min irradiation per time and carried out every three days. According to the extracted tumor photos and tumor growth curve, we found the NPs/DOX@GelMA/DMXAA +Laser (PT) group had the best therapeutic effect and the tumor volume gradually reduced until disappeared (Figure 6a,b; Figure S13a,b, Supporting Information). Meantime, the tumor weight results also showed that the microgel +Laser group had the lowest tumor weight (Figure 6c; Figure S13c, Supporting Information).

Moreover, the tumor inhibition rate (IR) was calculated by the following equation:

$$IR(\%) = (1 - T_{wt}/T_{wc}) \times 100 \quad (3)$$

where T_{wt} and T_{wc} are the mean tumor weight of treated and control groups, and the tumor suppression rate of the NPs/DOX@GelMA/DMXAA +Laser (PT) group was $94.5 \pm 5.5\%$ (Figure 6d). These results together implicated that the microgel system possessed strongest tumor growth inhibitory ability, which contributed by the long-term multi-round realization of precision chemo-antiangiogenesis-photothermal synergistic therapy and osteosarcoma cells enhanced uptake of ALN modified NPs/DOX.

Notably, compared with the pure drug and -Laser groups, DMXAA(PT) + NPs/DOX(IV) +Laser group also had a tumor

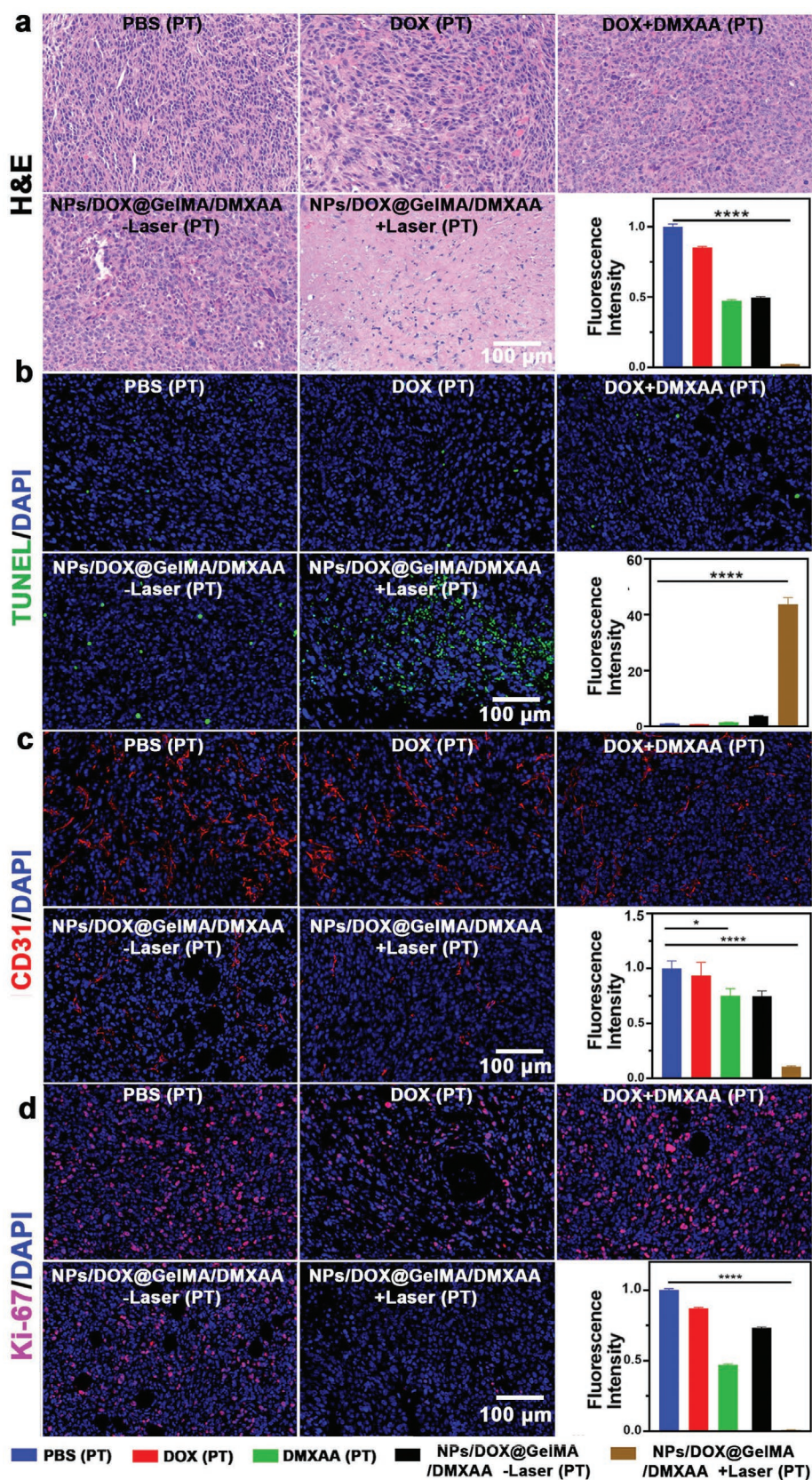


Figure 7. Histological analysis of tumors for different groups after peritumoral administration. a) H&E stained photos. b–d) DLSP imaging of TUNEL, Ki-67, CD31, and DAPI stained tumor sections (all bar equal to 100 μm , * $p < 0.05$, ** $p < 0.01$, *** $p < 0.001$, and **** $p < 0.0001$).

suppression effect, whereas the tumor volume still gradually increased. This was because that NPs/DOX through intravenous delivery had a better effect than the pure drug which is contributed by EPR effect and ALN receptor-mediated tumor cell enhanced uptake. However, when there was only single dose and only 20% of the normal dosage was used, the therapeutic effect was obviously not satisfactory and the tumor IR was only $58.5 \pm 7.3\%$ (Figure S13d, Supporting Information).

Moreover, the body weight and different organs (heart, liver, spleen, lung, and kidney) H&E staining picture of the mice were monitored for systemic safety evaluation. From the results, there was no significant difference between different groups about body weight (Figure 6e; Figure S13e, Supporting Information). Also for the H&E imaging, no obvious toxicity was found since the toxicity of high concentration was minimized (Figure S14, Supporting Information).

In order to further validate the tumor apoptosis and the inhibition degree of angiogenesis, the extracted tumor slices were further performed H&E, Ki-67, TUNEL, and CD31 staining for histological analysis. Very obvious nuclear shrinkage and cytosol degradation was found in the H&E stained tumor sections from NPs/DOX@GelMA/DMXAA +Laser group (Figure 7a). This result confirmed that this microgel system had the best tumor killing effect which can severely kill the tumor cells. Notably, several structure damages was also found in the H&E staining results from DMXAA(PT) + NPs/DOX(IV) +Laser group (Figure S15a, Supporting Information). This was because that the NPs/DOX can also kill the tumor cells after intravenous administration, since the NPs/DOX will accumulate in the tumor sites based on the EPR effect as well as possessing PTT and ALN receptor-mediated enhanced uptake at the same time. However, its drug delivery efficiency and retention ability were inferior to NPs/DOX-decorated microgel through peritumoral administration.

Furthermore, in the tumor slices from NPs/DOX@GelMA/DMXAA +Laser group, tremendous TUNEL signal and negligible Ki-67 signal was found, which means more apoptotic cells and less proliferating cells (Figure 7b,c). At the same time, DMXAA(PT) + NPs/DOX(IV) +Laser group also showed a certain degree of therapeutic effect compared with other groups, but its effectiveness was far less than that of NPs/DOX@GelMA/DMXAA +Laser group (Figure S15b,c, Supporting Information). Hence, the results of TUNEL signal and Ki-67 fluorescence were consistent with the results of H&E staining, which proved that the therapeutic effect of the microgel system was much better than that of the NPs group.

Later, CD31, as a typical vascular endothelial cell marker, was used to stain the tumor slices and assess the anti-angiogenesis degree.^[29] We can apparently see the CD31 red signal in the PBS (PT) and DOX (PT) group, which suggested strong tumor angiogenesis (Figure 7d). After DMXAA was peritumorally injected alone by a single dose, the expression of vascular marker CD31 in DMXAA (PT) group was reduced but not significant. However, for NPs/DOX@GelMA/DMXAA +Laser (PT) group, the blood vessels almost disappeared compared with the other groups, which was contributed to by the microgel based long-term multi-round drug release (Figure 7d; Figure S15d, Supporting Information). Therefore, this nanocomposite microgel system can not only achieve strong tumor suppression,

but also reduce blood vessel proliferation and prevent remote tumor metastasis.

3. Conclusion

In summary, with adjustable in situ retention and NIR-triggered receptor-mediated targeting ability, an ultra-efficient injectable nanocomposite microgel has been successfully prepared through a facile one-way microfluidic technology for repeated solid tumor chemo-photothermal therapy and angiogenesis inhibition. This novel dual-drug delivery system has demonstrated outstanding triple synergistic therapeutic effects in both in vitro and in vivo experiments. It is found that through a single administration, multiple rounds of light-controlled treatment can be achieved. Moreover, compared with intravenously administered nanosystems, this microgel can solve the shortcoming of insufficient targeting of NPs/DOX to solid tumors and significantly reduces the drug doses due to the PT regime and ALN mediated enhanced cell uptake. Furthermore, this microgel also possesses gratifying anti-capillary efficiency due to the long-term DMXAA vascular disturbing effect. In general, NPs/DOX@GelMA/DMXAA microgel is a promising drug delivery system for in situ administration for the treatment of solid tumors, which can allow a lower dosing regimen without losing the therapeutic effect and is thus promising for the treatment of solid tumors in the future.

4. Experimental Section

Seed@CTAB Preparation and Growth (AuNRs): Seed@CTAB was conducted according to a published protocol.^[30] Seed@CTAB was synthesized in a 30 °C water bath. First, 30 μ L of 50 mM HAuCl₄ solution was added to 5 mL of 0.1 M CTAB solution. After the solution was fully stirred for 5 min, 300 μ L of 10 mM NaBH₄ solution was injected. After that, another solution for NPs/DOX growth was prepared. First, 190 μ L HCl 1 M and 100 μ L HAuCl₄ 50 mM solution were added to 10 mL of 0.1 M CTAB. Adjust the pH to 1.5 by HCL. Then 120 μ L of AgNO₃ containing 10 mM and 100 μ L of ascorbic acid solution (100 mM) were added to the above solution. Finally, 24 μ L of the previously prepared Seeds@CTAB was added to the growth solution, stirred well and let stand at 30 °C for 2 h.

SiO₂ Coating (AuNR@SiO₂): Mesoporous silica coating on AuNRs was carried out according to a published protocol.^[37] The AuNRs prepared above were centrifuged at 15 000 g for 25 min, washed 3 times with Milli-Q water, and finally diluted to 20 mL with water. Then 200 μ L of 0.1 M NaOH solution was added under stirring. Subsequently, every 30 min, 60 μ L of 20% TEOS methanol solution was added to the above solution for a total of 3 times. Finally, the reaction continued for 3 days at room temperature. Later, -NH₂ modification (AuNR@SiO₂-NH₂) and -COOH modification (AuNR@SiO₂-COOH) were carried out according to the published protocol^[9,21] and described in the Supporting Information.

DOX Loading and ALN Surface Modification (DOX@AuNR@SiO₂-ALN): 10 mg of DOX and AuNR@SiO₂ nanoparticles which contained 10 mg of AuNRs were blended within 10 mL Milli-Q water, and stirred vigorously on a magnetic stirrer. After 24 h of drug loading, the NPs/DOX were centrifuged at 10 000 g and washed with ethanol three times. Then, the drug loaded DOX@AuNR@SiO₂-COOH NPs were put into 10 mL Milli-Q water, 0.1 mg NHS and 0.1 mg EDC were added together into the solution and stirred 1 h for carboxyl group activation. Subsequently, 10 mg of ALN was added and reacted with NPs/DOX for another 24 h at room temperature. Finally, NPs/DOX were centrifuged

at 10 000 g and washed with Milli-Q water for three times. The DOX LC and loading efficiency (LE) were calculated according to the following Equations (4) and (5):

$$LC(\%) = \frac{\text{entrapped drug}}{\text{weight of nanoparticles}} \times 100\% \quad (4)$$

$$LE\% = \frac{\text{total input of drug} - \text{amount of drug in the supernatant}}{\text{total input of drug}} \quad (5)$$

Measurement of Photothermal Performance: For measuring the photothermal conversion ability of the DOX@AuNR@SiO₂-ALN nanoparticles, three experiments were conducted. First, 1 mL aqueous dispersion of NPs/DOX with different concentrations (0, 0.25, 5, and 1 mg mL⁻¹) were introduced in a quartz cuvette and irradiated with an 980 nm NIR laser at a power density of 1 W cm⁻² for 300 s, and the thermal imaging pictures were simultaneously recorded by thermal imaging cameras. Second, 1 mL aqueous dispersion of NPs/DOX with same concentrations (1 mg mL⁻¹) were prepared in a quartz cuvette and irradiated at different power density (0.5, 1, and 1.5 W cm⁻²) for 300 s, respectively. Third, a heating-cooling cycles experiments was determined by using 1 mg mL⁻¹ NPs/DOX solutions and continually irradiated with a 1 W cm⁻² 980 nm NIR laser to the plateau temperature. Then it was cooled down naturally to the room temperature. A thermocouple probe with an accuracy of 0.1 °C was inserted into the upper mentioned DOX@AuNR@SiO₂-ALN aqueous solution. The temperature was recorded every 30 s by a digital thermometer.

NIR Triggered Pulsated Drug Release Experiment: The drug release experiment was divided into two groups, one was the laser group and the other was the without laser group. The release experiment of the two groups was all carried out in 1 mL PBS solution in a shaker at 37 °C, and all contained DOX@AuNR@SiO₂-ALN NPs/DOX which equally containing 0.5 mg AuNRs. For the laser group, the nanoparticles were irradiated with 1 W cm⁻² laser for 5 min at 2, 4, and 5 h. At each time point for both groups, solutions were centrifuged and the 0.9 mL of supernatant was taken out for drug concentration testing, then 0.9 fresh PBS also added back and dispersed well before putting back to the shaker.

GelMA Preparation: 20 g^[38] of gelatin was weighed and dispersed into 200 mL PBS (0.01 M). Then the procedure was carried within a water bath to make the temperature of gelatin reach 60 °C and stirred until dissolution was clear. Later, a syringe was used to draw 16 mL of MA and slowly added MA to the gelatin by using a micro syringe pump at a speed of 0.25 mL min⁻¹. After adding MA for 2 h, 200 mL PBS was then added to stop the reaction. After the reaction was terminated for 15 min, GelMA was put into a dialysis bag (MWCO 3500), dialyzed overnight at 38 °C, then centrifuged at 10 000 g for 15 min at 37 °C to remove insolubles, the supernatant was taken and dialysis was continued for 2–3 days. The GelMA was finally dispensed into multiple plates, and placed them in a minus 80 refrigerator for storage before lyophilized.

Microgel Preparation (NPs/DOX@GelMA/DMXAA): First^[39,40] 150 mg of lyophilized GelMA and 15 mg of photocrosslinker were dissolved into 3 mL of 0.1 M PBS. Then 1 mL of the above solution was taken and 9 mg DMXAA was added and ultrasonic at 60 °C for 30 min until it dispersed evenly. Then 10 mg NPs/DOX were added and dispersed again, finally the aqueous phase was prepared. Later the oil phase was also prepared by adding 5% Span 80 to the mineral oil. The aqueous phase and oil phase were co-flowed in a microfluidic droplet chips which was purchased from MesoBioSystem Company (Wuhan, China). Different flow rate of different liquids was controlled by a pump (PHD 2000, Harvard Apparatus, USA). A UV lamp was fixed on the droplets collection bottle, and the GelMA droplets will be crosslinked under the UV irradiation. Then the microgels were collected by centrifuged at 300 g and washed three times with 75% ethanol. The size of the obtained microgels was measured under NIH ImageJ software based on the pictures taken by the microscope.

NIR Triggered Accelerated Drug Release Experiment: NPs/DOX@GelMA/DMXAA^[41] microgel which equally containing 1 mg AuNRs was added to 1 mL Milli-Q water. Every three days, the solution was centrifuged and the supernatant was taken out to measure the drug concentrations of DOX and DMXAA, and the cumulative release of these two drugs were calculated separately. During the time, on the 6th and 12th day, 980 nm laser with 1 W cm⁻² was used to irradiate the microgel for 10 min.

In Vitro: Human osteosarcoma (MNNG/HOS) cells and HUVEC cells were provided by Department of Central Laboratory, The Second Hospital of Jiaxing (China). MNNG/HOS cells were grown in DMEM medium containing 10% FBS, 1% penicillin, and streptomycin. HUVEC cells were grown in 1640 medium containing 10% FBS, 1% penicillin, and streptomycin. The detailed steps of cell experiments including Cytotoxicity, CLSM Imaging, Calcein/PI Cell Viability/Cytotoxicity Assay, Annexin V-FITC cell apoptosis detection, and Tube formation experiments are described in the Supporting Information.

In Vivo: All experiments including animal operations were approved by the Animal Research Committee of Ruijin Hospital, Shanghai Jiao Tong University School of Medicine, China. The MNNG/HOS cells were cultured in large quantities around 40 bottles in the cell culture bottle (1 × 10⁷ cells per bottle). After the cells were grown sufficiently, each bottle of cells (1 × 10⁷ cells) was diluted with 100 µL cell medium and injected into the subcutaneous of axilla of BALB/c-nu nude mice. All nude mice were 6-week-old female mice. After weighing, the mice were evenly divided into seven groups according their weight for the tumor suppression test. The tumor volume was observed and recorded every day. The administration method for later treatment was divided into PT and tail vein injection (IV). When the tumor volume reached about 80 mm³, mice were divided into 7 groups including PBS (PT), DOX (PT), DMXAA (PT), DMXAA (PT) +NPs/DOX (IV) –Laser, DMXAA (PT) +NPs/DOX (IV) +Laser, NPs/DOX/DOX@GelMA/DMXAA (PT) –Laser, and NPs/DOX/DOX@GelMA/DMXAA (PT) +Laser group, and each group contained four mice. The in vivo experiments including In Vivo IR Thermo-imaging, In Vivo Fluorescence Imaging, In Vivo Anticancer Efficacy, H&E staining, and TUNEL, Ki-67, CD31 staining for tumor slices. The details for each experiment are explained in the Supporting Information.

Supporting Information

Supporting Information is available from the Wiley Online Library or from the author.

Acknowledgements

J.Y., Y.W., and M.R. contributed equally to this work. This work was supported by grants from the National Nature Science Foundation of China (81871472, 81772393), Beijing Municipal Natural Science Foundation (7192214), Special Project of Integrated Traditional Chinese and Western Medicine in General Hospitals of Shanghai (ZHYX-ZXYJHZX-201901), Academy of Finland (309374 and 328933), and Sigrid Jusélius Foundation.

Conflict of Interest

The authors declare no conflict of interest.

Data Availability Statement

Research data are not shared.

Keywords

modulatable biodegradability, nanocomposite microgel, osteosarcoma targeting, triple-synergetic therapy, ultra-low dosage

Received: January 25, 2021

Revised: May 16, 2021

Published online:

- [1] A. I. Minchinton, I. F. Tannock, *Nat. Rev. Cancer* **2006**, *6*, 583.
- [2] H. Zhang, Y. Zhu, L. Qu, H. Wu, H. Kong, Z. Yang, D. Chen, E. Makila, J. Salonen, H. A. Santos, M. Hai, D. A. Weitz, *Nano Lett.* **2018**, *18*, 1448.
- [3] F. Zhang, A. Correia, E. Makila, W. Li, J. Salonen, J. J. Hirvonen, H. Zhang, H. A. Santos, *ACS Appl. Mater. Interfaces* **2017**, *9*, 10034.
- [4] H. Zhang, D. Liu, M. A. Shahbazi, E. Makila, B. Herranz-Blanco, J. Salonen, J. Hirvonen, H. A. Santos, *Adv. Mater.* **2014**, *26*, 4497.
- [5] S. Qi, P. Zhang, M. Ma, M. Yao, J. Wu, E. Makila, J. Salonen, H. Ruskoaho, Y. Xu, H. A. Santos, H. Zhang, *Small* **2019**, *15*, 1804332.
- [6] T. Yong, X. Zhang, N. Bie, H. Zhang, X. Zhang, F. Li, A. Hakeem, J. Hu, L. Gan, H. A. Santos, X. Yang, *Nat. Commun.* **2019**, *10*, 3838.
- [7] G. Ni, G. Yang, Y. He, X. Li, T. Du, L. Xu, S. Zhou, *Chem. Eng. J.* **2020**, *379*, 122317.
- [8] X. Zhou, X. He, K. Shi, L. Yuan, Y. Yang, Q. Liu, Y. Ming, C. Yi, Z. Qian, *Adv. Sci.* **2020**, *7*, 2001442.
- [9] J. Yan, C. Liu, Q. Wu, J. Zhou, X. Xu, L. Zhang, D. Wang, F. Yang, H. Zhang, *Anal. Chem.* **2020**, *92*, 11453.
- [10] H. Zhang, W. Cui, X. Qu, H. Wu, L. Qu, X. Zhang, E. Makila, J. Salonen, Y. Zhu, Z. Yang, D. Chen, H. A. Santos, M. Hai, D. A. Weitz, *Proc. Natl. Acad. Sci. USA* **2019**, *116*, 7744.
- [11] Y. Liang, Y. Wang, L. Wang, Z. Liang, D. Li, X. Xu, Y. Chen, X. Yang, H. Zhang, H. Niu, *Bioact. Mater.* **2021**, *6*, 433.
- [12] B. Liu, J. Sun, J. Zhu, B. Li, C. Ma, X. Gu, K. Liu, H. Zhang, F. Wang, J. Su, Y. Yang, *Adv. Mater.* **2020**, *32*, 2004460.
- [13] Z. Meng, Y. Chao, X. Zhou, C. Liang, J. Liu, R. Zhang, L. Cheng, K. Yang, W. Pan, M. Zhu, Z. Liu, *ACS Nano* **2018**, *12*, 9412.
- [14] R. A. Sheth, R. Murthy, D. S. Hong, S. Patel, M. J. Overman, A. Diab, P. Hwu, A. Tam, *JAMA Network Open* **2020**, *3*, e207911.
- [15] L. Zhang, H. Su, J. Cai, D. Cheng, Y. Ma, J. Zhang, C. Zhou, S. Liu, H. Shi, Y. Zhang, C. Zhang, *ACS Nano* **2016**, *10*, 10404.
- [16] D. Guo, Y. Huang, X. Jin, C. Zhang, X. Zhu, *Biomaterials* **2021**, *266*, 120400.
- [17] S. Geng, H. Zhao, G. Zhan, Y. Zhao, X. Yang, *ACS Appl. Mater. Interfaces* **2020**, *12*, 7995.
- [18] D. Bartczak, O. L. Muskens, S. Nitti, T. M. Millar, A. G. Kanaras, *Biomater. Sci.* **2015**, *3*, 733.
- [19] H. Song, T. Guo, Z. Zhao, Y. Wei, H. Luo, W. Weng, R. Zhang, M. Zhong, C. Chen, J. Su, W. Shen, *Biomaterials* **2018**, *178*, 23.
- [20] S. H. Chen, T. I. Liu, C. L. Chuang, H. H. Chen, W. H. Chiang, H. C. Chiu, *J. Mater. Chem. B* **2020**, *8*, 3789.
- [21] H. Ren, S. Chen, Y. Jin, C. Zhang, X. Yang, K. Ge, X. J. Liang, Z. Li, J. Zhang, *J. Mater. Chem. B* **2017**, *5*, 1585.
- [22] J. Yang, Y. Zhu, F. Wang, L. Deng, X. Xu, W. Cui, *Chem. Eng. J.* **2020**, *400*, 126004.
- [23] R. Cheng, L. Liu, Y. Xiang, Y. Lu, L. Deng, H. Zhang, H. A. Santos, W. Cui, *Biomaterials* **2020**, *232*, 119706.
- [24] H. Wang, A. J. Najibi, M. C. Sobral, B. R. Seo, J. Y. Lee, D. Wu, A. W. Li, C. S. Verbeke, D. J. Mooney, *Nat. Commun.* **2020**, *11*, 5696.
- [25] F. Gao, Z. Xu, Q. Liang, H. Li, L. Peng, M. Wu, X. Zhao, X. Cui, C. Ruan, W. Liu, *Adv. Sci.* **2019**, *6*, 1900867.
- [26] W. Tang, Y. Yu, J. Wang, H. Liu, H. Pan, G. Wang, C. Liu, *Biomaterials* **2020**, *232*, 119645.
- [27] J. Lee, V. Manoharan, L. Cheung, S. Lee, B. H. Cha, P. Newman, R. Farzad, S. Mehrotra, K. Zhang, F. Khan, M. Ghaderi, Y. D. Lin, S. Aftab, P. Mostafalu, M. Miscuglio, J. Li, B. B. Mandal, M. A. Hussain, K. T. Wan, X. S. Tang, A. Khademhosseini, S. R. Shin, *ACS Nano* **2019**, *13*, 12525.
- [28] W. Wu, Y. Dai, H. Liu, R. Cheng, Q. Ni, T. Ye, W. Cui, *Drug Delivery* **2018**, *25*, 1642.
- [29] D.-W. Z. Sheng Hong, C. Zhang, Q.-X. Huang, S.-X. Cheng, X.-Z. Zhang, *Sci. Adv.* **2020**, *6*, eabb0020.
- [30] L. Scarabelli, A. Sanchez-Iglesias, J. Perez-Juste, L. M. Liz-Marzan, *J. Phys. Chem. Lett.* **2015**, *6*, 4270.
- [31] J. Hu, H. Luo, Q. Qu, X. Liao, C. Huang, J. Z. Y. Bao, G. Chen, B. Li, W. Cui, *ACS Appl. Mater. Interfaces* **2020**, *12*, 42511.
- [32] X. Sun, Q. Lang, H. Zhang, L. Cheng, Y. Zhang, G. Pan, X. Zhao, H. Yang, Y. Zhang, H. A. Santos, W. Cui, *Adv. Funct. Mater.* **2017**, *27*, 1604617.
- [33] X. Zhao, S. Liu, L. Yildirimer, H. Zhao, R. Ding, H. Wang, W. Cui, D. Weitz, *Adv. Funct. Mater.* **2016**, *26*, 2809.
- [34] L. Tamayo, D. Acuna, A. L. Riveros, M. J. Kogan, M. I. Azocar, M. Paez, M. Leal, M. Urzua, E. Cerda, *ACS Appl. Mater. Interfaces* **2018**, *10*, 13361.
- [35] G. Carpentier, S. Berndt, S. Ferratge, W. Rasband, M. Cuendet, G. Uzan, P. Albanese, *Sci. Rep.* **2020**, *10*, 11568.
- [36] J. He, C. Li, L. Ding, Y. Huang, X. Yin, J. Zhang, J. Zhang, C. Yao, M. Liang, R. P. Pirraco, J. Chen, Q. Lu, R. Baldrige, Y. Zhang, M. Wu, R. L. Reis, Y. Wang, *Adv. Mater.* **2019**, *31*, 1902409.
- [37] I. G. N. Matsuura, *Nano Lett.* **2007**, *8*, 369.
- [38] L. Shao, Q. Gao, H. Zhao, C. Xie, J. Fu, Z. Liu, M. Xiang, Y. He, *Small* **2018**, *14*, 1802187.
- [39] J. Bian, F. Cai, H. Chen, Z. Tang, K. Xi, J. Tang, L. Wu, Y. Xu, L. Deng, Y. Gu, W. Cui, L. Chen, *Nano Letters* **2021**, *21*, 2690.
- [40] J. Yan, X. Xu, J. Zhou, C. Liu, L. Zhang, D. Wang, F. Yang, H. Zhang, *ACS Appl. Bio Mater.* **2020**, *3*, 1216.
- [41] H. Luo, L. Kong, F. Zhang, C. Huang, J. Chen, H. Zhang, H. Yu, S. Zheng, H. Xu, Y. Zhang, L. Deng, G. Chen, H. A. Santos, W. Cui, *Adv. Funct. Mater.* **2021**, 2101262, <https://doi.org/10.1002/adfm.202101262>.